Common-path and compact wavefront diagnosis system based on cross grating lateral shearing interferometer

Tong Ling, Yongying Yang,* Xiumei Yue, Dong Liu, Yifang Ma, Jian Bai, and Kaiwei Wang

State Key Laboratory of Modern Optical Instrumentation, Zhejiang University, 38 Zheda Road, Hangzhou 310027, China

*Corresponding author: chuyyy@zju.edu.cn

Received 7 August 2014; revised 14 September 2014; accepted 17 September 2014; posted 18 September 2014 (Doc. ID 220528); published 17 October 2014

A common-path and compact wavefront diagnosis system for both continuous and transient wavefronts measurement is proposed based on cross grating lateral shearing interferometer (CGLSI). Derived from the basic CGLSI configuration, this system employs an aplanatic lens to convert the wavefront under test into a convergent beam, which makes it possible for CGLSI to test the wavefront of collimated beams. A geometrical optics model for grating pitch determination and a Fresnel diffraction model for order selection mask design are presented. Then a detailed analysis about the influence of the grating pitch, the distance from the cross grating to the order selection mask and the numerical aperture of the aplanatic lens on the system error is made, and a calibration method is proposed to eliminate the system error. In addition, the differential Zernike polynomials fitting method is introduced for wavefront retrieval. Before our experiment, we have designed several grating pitches and their corresponding order selection mask parameters. In the final comparative experiment with ZYGO interferometer, the wavefront diagnosis system exhibits both high precision and repeatability. © 2014 Optical Society of America

OCIS codes: (120.0120) Instrumentation, measurement, and metrology; (120.3180) Interferometry; (050.1950) Diffraction gratings; (120.5050) Phase measurement.

http://dx.doi.org/10.1364/AO.53.007144

1. Introduction

During the generation or propagation process of light beams, the wavefront of a beam will be distorted due to different factors; for example, the figure of the optical surfaces in the optical path, air disturbance, defects of the optical materials, and variation of temperature and stress in the propagation medium will all result in the wavefront distribution's difference. In general, this difference in wavefront distribution will definitely reduce the quality of light beams. However, on the other hand, it also records the figure of the optical surfaces that the beams strike and the characteristics of the optical materials the beams pass through. The performance of the actual imaging system can be obtained from the wavefront aberration as well. Therefore, the diagnosis of wavefront distortion is widely employed in many fields, such as precision optics fabrication, adaptive optics system of large telescopes, high power lasers in inertial confinement fusion (ICF) systems, and hypersonic flow field testing.

The most commonly used methods at present for wavefront measurement are interferometry and Hartmann wavefront sensors, among which the Hartmann or Shack–Hartmann sensors are mainly based on the measurement of wavefront slope in different parts of the aperture with a grating at the Talbot distance or a micro lens array. The Hartmann wavefront sensors have a large dynamic range, but the sampling resolution is relatively lower than

1559-128X/14/307144-09$15.00/0

the resolution of interferometry [1,2]. Conventional interferometry, like Fizeau and Twyman–Green interferometer, employs a phase shifting method by introducing a time-varying phase shift between the reference wavefront and the test wavefront for phase retrieval and eliminating the random noise in the test result, which is highly precise. But the disadvantage of using the time-varying phase shifting method is that it needs multiple interferograms to retrieve the wavefront under test so it can only test the continuous laser beams. Therefore, based on the Fizeau and Twyman–Green interferometer, one-shot phase shifting interferometers such as the 4D interferometer are proposed, which is able to obtain at least four interferograms simultaneously from one single CCD image with the modulation of polarization and, as a result, is capable of measuring transient pulse wavefronts [3–7]. One of the costs of these one-shot phase shifting interferometers is that the testing resolutions will be lower than before, as one CCD image is divided into at least four subimages. In addition, a precisely fabricated reference flat is also needed by the interferometry based on the Fizeau or Twyman–Green interferometer, and the finesse of that reference flat will directly determine the precision of the test result.

Thanks to the self-reference characteristics, there is no need for shearing interferometers to introduce the absolute reference flat [8]. Usually, there are two types of shearing interferometers; one is a lateral shearing interferometer and the other is a radial shearing interferometer. A cyclic radial shearing interferometer is capable of testing both continuous and pulse laser beams, and it shows high precision and repeatability due to its common-path feature. However, the mechanical structure of a cyclic radial shearing interferometer is large and it takes up a lot of space [9–11]. Actually, a lateral shearing interferometer is comparatively more compact, and the lateral shearing interferometers that are able to test the transient wavefront include the cross grating lateral shearing interferometer (CGLSI) [12–17], the three-wave lateral shearing interferometer (TWLSI) [18,19], and the quadriwave lateral shearing interferometer (QWLSI) [20–24]. Among them, the TWLSI and QWLSI are both based on the phase grating, and different types of errors may be introduced during the fabricating process of the phase grating [25]. Relatively speaking, the fabrication of the cross grating is more simple and accurate. Taking advantage of the common-path and self-reference features, the CGLSI is able to suppress the environment vibration and retrieve the wavefront under test from only a single interferogram, so it can be applied to both continuous and transient wavefront testing.

In this paper, a common-path and compact wavefront diagnosis system for both continuous and transient wavefront measurement based on a CGLSI is proposed. Section 2 describes the system layout of this interferometer. The detailed mathematical modeling of a CGLSI and the analysis of the grating pitch in relation to shear ratio is given; the position and the size of the order selection windows are precisely calculated using Fresnel diffraction theory in Section 3. Section 4 mainly presents the analysis of the system error in this diagnosis system and its calibration. The wavefront retrieval method using differential Zernike polynomials fitting is introduced in Section 5. The design parameters of cross grating and order selection windows are given in Section 6, while the comparative experiments between the CGLSI and ZYGO interferometer to examine the same wavefront under test are also presented, which show that the repeatability of the wavefront diagnosis system based on the CGLSI are relative higher.

2. Basic Principle

The common-path and compact wavefront diagnosis system based on a CGLSI consists of an aplanatic lens, a cross grating, an order selection mask, and a CCD, as shown in Fig. 1. During the measurement process, the wavefront under test first goes through an aplanatic lens and becomes a convergent beam. Then, it strikes the cross grating and is diffracted into multiple orders in the x and y directions. The order selection mask placed at the focal plane is used to select the ± 1st diffraction orders in the x and y directions and let these 4 orders pass through. These beams will finally reach the CCD imaging plane and form a cross grating lateral shearing interferogram in their overlapped region.

The interferogram on the CCD contains both shearing wavefronts in the x and y directions, and the wavefront under test can be obtained with the help of the fast Fourier transform (FFT) and differential Zernike polynomials fitting method. Here, the FFT is employed to get the frequency spectrum of the interferogram. By performing inverse fast Fourier transform (IFFT) of the $+1$ order spectrum in both x and y directions, it is possible to extract shearing wavefronts in these two orthogonal directions from the interferogram. Then, utilizing the differential Zernike polynomial fitting method, we are able to integrate these shearing wavefronts together and retrieve the wavefront under test.

The CGLSI wavefront diagnosis system is compact in structure, but the grating pitch and the parameters of windows on the order selection mask remain

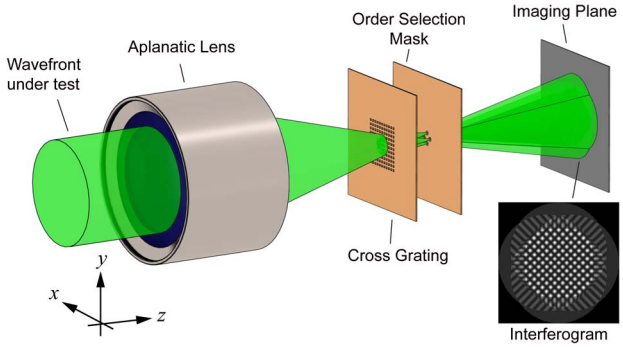

Fig. 1. System layout of CGLSI wavefront diagnosis system.

fixed once they have been fabricated. It is impossible to readjust these parameters to image the desired interferogram on CCD in the testing process, and all the parameters of different parts of the system must be correctly and precisely predetermined before testing. Therefore, the mathematical model of the CGLSI that considers all these parameters should be first established.

3. Mathematical Modeling of CGLSI

The schematics of the CGLSI wavefront diagnosis system is shown in Fig. 2. As we focus to analyze the y–z plane, only two diffraction orders are considered in this model. Assume that D is the aperture of the wavefront under test, f is the focal length of the aplanatic lens, l_1 is the distance between the lens and the cross grating, d is the pitch of cross grating, l_2 is the distance between the cross grating and the order selection mask, l_3 is the distance from the selection mask to the imaging plane, d_{win} is the distance between the center of two windows in the x or the y direction on the order selection mask, and D_{win} is the diameter of each window. The analysis and determination of the shear-ratio-related grating pitch, d, the position and the size of the windows on the order selection mask, d_{win} and D_{win}, will be described as follows based on the mathematical modeling of the CGLSI.

A. Shear-Ratio-Related Grating Pitch

The most important parameter to the lateral shearing interferometer is the shear ratio, β, which greatly affects the amount of wavefront information obtained. While the shear ratio, β, increases, the area of the actual interference region decreases. The shear ratio is usually defined as the shear amount, s, between two shearing wavefronts in the same direction, divided by the diameter, T, of one shearing wavefront on the imaging plane, that is

$$\beta = \frac{s}{T}. \tag{1}$$

In order to obtain the expression of the shear amount, s, we can first analyze the distance between the spots, P_{+1} and P_{-1}, of the $+1$ and the -1

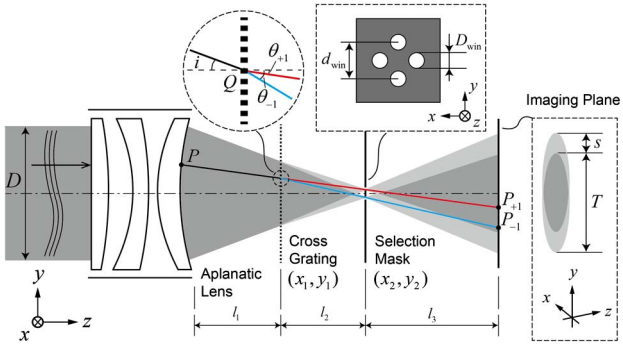

Fig. 2. Schematic diagram of the CGLSI wavefront diagnosis system.

diffractions on the imaging plane, which comes from the same light ray. So consider that the ray passes through the point, P. which is located on the rear surface of the aplanatic lens, as is shown in Fig. 2. Assume that the coordinate of the point, P, is $(0, y_P)$, and the incident angle, i, of the ray striking on the cross grating can be expressed as

$$i = \arctan \frac{y_P}{f}. \tag{2}$$

The coordinate of the point, Q, that this ray strikes on the cross grating front surface is

$$\begin{aligned} x_Q &= 0, \\ y_Q &= y_P - l_1 \tan i. \end{aligned} \tag{3}$$

According to the diffraction grating equation, the exit angle, θ_{+1} and θ_{-1}, of the ± 1 order diffractions can be described as

$$\begin{aligned} d \sin i + d \sin \theta_{+1} &= \lambda, \\ d \sin i - d \sin \theta_{-1} &= -\lambda. \end{aligned} \tag{4}$$

the position of each diffraction spot, P_{+1} or P_{-1}, on the imaging plane is

$$\begin{aligned} y_{P_{+1}} &= y_Q + (l_2 + l_3) \tan \theta_{+1}, \\ y_{P_{-1}} &= y_Q - (l_2 + l_3) \tan \theta_{-1}. \end{aligned} \tag{5}$$

For the simplicity of calculation, we can make an approximation of trigonometric functions when the numerical aperture of the aplanatic lens, NA, is less than 0.2, that is

$$\begin{aligned} \sin i &= \tan i = i, \\ \sin \theta_{+1} &= \tan \theta_{+1} = \theta_{+1}, \\ \sin \theta_{-1} &= \tan \theta_{-1} = \theta_{-1}. \end{aligned} \tag{6}$$

Then the shear amount, s, can be obtained by combining Eqs. (2)–(6),

$$s = y_{P_{+1}} - y_{P_{-1}} = 2(l_2 + l_3)\frac{\lambda}{d}. \tag{7}$$

From geometry, the diameter, T, of the shearing wavefront on the imaging plane is

$$T = (l_1 + l_2 + l_3)\frac{D}{f} - D. \tag{8}$$

Substituting Eqs. (7) and (8) into Eq. (1), the shear ratio, β, can be obtained as

$$\beta = \frac{2(l_2 + l_3)\frac{\lambda}{d}}{(l_1 + l_2 + l_3)\frac{D}{f} - D}. \tag{9}$$

As the interferogram should be fully imaged on the CCD plane, the size of the overlapped region among shearing wavefronts should be equal to the height of CCD active area, so the constraint of the field of view (FOV) of CCD can be expressed as

$$h = -2(l_2 + l_3)\frac{\lambda}{d} - D + (l_1 + l_2 + l_3)\frac{D}{f}. \tag{10}$$

The wavelength, λ, of the beam under test, the height, h, of FOV, the distance, l_1, from the aplanatic lens to the cross grating and the distance, l_2, from the cross grating to the order selection mask are all fixed during the measuring process, but the distance, l_3, from the order selection mask to CCD imaging plane has to be determined by adjusting CCD to a certain position where the full interferogram can be obtained. From Eq. (10), we can get

$$l_3 = \frac{h + \frac{2l_2\lambda}{d} - (l_1 + l_2)\frac{D}{f} + D}{\frac{D}{f} - \frac{2\lambda}{d}}. \tag{11}$$

After the determination of l_3, the final shear ratio, β, can be obtained from Eqs. (9) and (10),

$$\beta = \frac{2(l_2 + l_3)\lambda}{hd + 2(l_2 + l_3)\lambda}, \tag{12}$$

where all the parameters except the grating pitch, d, is determinate. Given the value $\lambda = 532$ nm, $D = 30$ mm, NA $= 0.15$, $h = 4.8$ mm, $l_2 = 1$ mm, the variation of the shear ratio, β, in relation to the grating pitch, d, is shown in Fig. 3, where the shear ratio gradually goes down as the pitch increases. From this figure, we are able to determine the right value of grating pitch according to the shear ratio we desire.

B. Parameters of Order Selection Mask

The incoming beam is diffracted by the cross grating in our wavefront diagnosis system into multiple diffractions, but we want only the ± 1 orders in the x and y directions. Therefore, an order selection mask is placed at the focal plane to let only the four diffraction beams pass through. The benefits of using the order selection mask are that not only the higher diffraction orders but also the zero-order are blocked, which gives a better contrast in the interferogram. Now, the analysis and design of the window position and size are carried out based on the determination of the grating pitch, d, and each distance, l_1, l_2, and l_3 between every two adjacent components above.

The convergent beam exiting from the aplanatic lens will first go through the cross grating, and different rays strike the grating with different incident angles, which result in the difference of positions that these rays hit on the focal plane. Therefore, the position of the order selection window cannot be simply determined with only the position of the chief ray or the marginal ray. To precisely analyze the position and size of diffraction spots on the focal plane, a numerical calculation based on wave optics theory is introduced [26]. As shown in Fig. 4, the model of the intensity distribution on the order selection mask is established in the theory of Fresnel diffraction.

Suppose that the complex amplitude distribution, $U_1(x_1, y_1)$, on the front surface of the cross grating can be expressed as

$$U_1(x_1, y_1) = \frac{1}{i\lambda(f - l_1)} \exp[ik(l_1 - f)] \exp\left\{ik\frac{x_1^2 + y_1^2}{2(l_1 - f)}\right\}. \tag{13}$$

Then, the amplitude $U_1'(x_1, y_1)$ on the rear surface of the cross grating is

$$U_1'(x_1, y_1) = U_1(x_1, y_1) \cdot t(x_1, y_1), \tag{14}$$

where $t(x_1, y_1)$ is the transmittance distribution of cross grating, that is,

$$t(x_1, y_1) = \left[\mathrm{rect}\left(\frac{2x_1}{d}\right) * \frac{1}{d}\mathrm{comb}\left(\frac{x_1}{d}\right)\right] \cdot \left[\mathrm{rect}\left(\frac{2y_1}{d}\right) * \frac{1}{d}\mathrm{comb}\left(\frac{y_1}{d}\right)\right]. \tag{15}$$

The complex amplitude, $U_2(x_2, y_2)$, on the order selection mask can be obtained as follows according to the Fresnel diffraction equation,

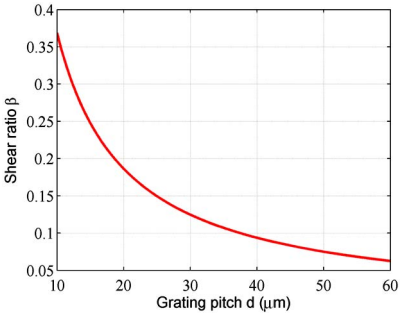

Fig. 3. Relationship between the shear ratio, β, and the grating pitch, d.

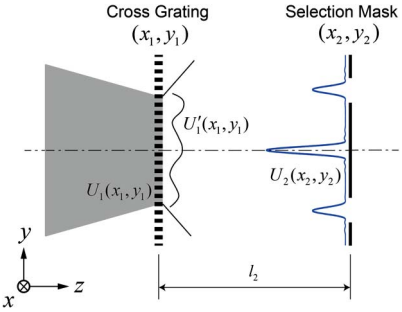

Fig. 4. Modeling of the intensity distribution on the order selection mask based on Fresnel diffraction theory.

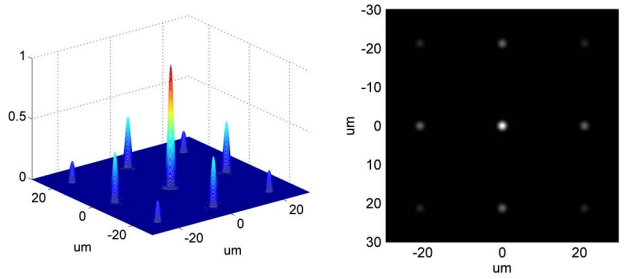

Fig. 5. Normalized intensity distribution on the selection mask: (a) 3D contour map and (b) grayscale image used for position locating.

$$U_2(x_2,y_2)=\frac{\exp(ikl_2)}{i\lambda l_2}\iint U_1'(x_1,y_1)\times\exp\left\{\frac{ik}{2l_2}[(x_2-x_1)^2+(y_2-y_1)^2]\right\}\mathrm{d}x_1\mathrm{d}y_1. \tag{16}$$

Substitute the actual values into Eq. (16) and the intensity distribution can finally be obtained. When the grating pitch, d, is 25 um and the aperture of the wavefront to be examined is 30 mm, the normalized intensity distribution on the focal plane is shown in Fig. 5, from which we can clearly identify the zero-order, the ±1 orders in both x and y directions, and the orders in the 45-deg directions. As the positions of the orders are easily to be figured out, the distance, d_{win}, of the selection windows can then be obtained with the peak intensity position of the ±1 orders, and the size of windows, D_{win}, should guarantee that all of ±1 orders will get through while other orders will be blocked.

4. System Error and Its Calibration

As the cross grating does not fit the perfect imaging condition, its participation will evidently introduce the axis aberrations into the wavefront diagnosis system. If the aplanatic lens is replaced by an ideal paraxial lens, the wavefront aberration on the focal point of this paraxial lens is 0. However, when the cross grating is brought into the system, all the rays will be deflected from their original path and different rays enter the cross grating with different incident angles, which will cause the coma aberration on the focal point. Moreover, astigmatism may also be introduced in the wavefront aberration on the focal point due to the asymmetry of optical paths in the x and the y directions. In fact, the analysis of the aberration on the focal point will indicate the size of system error, whether it is large or small, and three different parameters, which are the grating pitch, d, the distance, l_2 from the cross grating to the focal plane (or the order selection mask) and the numerical aperture of the aplanatic lens, NA, will all affect this focal plane aberration. Given that the wavelength, $\lambda=532$ nm, the aperture of the wavefront tested, $D=30$ mm, and supposing the grating pitch, $d=25$ μm, the numerical aperture of the aplanatic lens, NA $=0.15$, and the distance between the cross grating and the focal plane, $l_2=1$ mm, we can analyze the influence of these three parameters on the focal plane aberration by varying one of them and making others stable.

A. Influence of Grating Pitch on the Focal Plane Aberration

Let us vary the grating pitch, d, from 20 to 60 μm and make an observation of the focal plane aberration with the help of ZEMAX. The flowchart about how to calculate the wavefront aberration is shown in Fig. 6. First the simulation model is built in ZEMAX, while the stop, the paraxial lens, the diffraction grating, and the imaging plane are sequentially placed in this model. Given the right parameters, as we mentioned above, and making the distance, l_1, between the paraxial lens and the diffraction grating variable, we can precisely locate the imaging plane on the focal plane with the optimization of l_1 regarding the wavefront on the imaging plane as the default merit function. Then, change the grating pitch, d, locate the right position of the focal plane with optical optimization, and record the peak-to-valley (PTV) and root-mean-square (RMS) values of the focal plane wavefront aberration. Eventually, the curve that indicates the variation of the focal plane aberration along with the variation of grating pitch is shown in Fig. 7(a). We can see that the smaller the grating pitch is, the larger the wavefront aberration, as the ray deflection effect of the cross grating is getting more and more obvious.

B. Influence of the Distance from the Grating to the Order Selection Mask on the Focal Plane Aberration

Utilizing the similar simulation method proposed in Section 4.A, we can obtain the curve showing the variation of the focal plane aberration with the change of the distance from the grating to the order selection mask, which is illustrated in Fig. 7(b). Here, the wavefront aberration on the focal plane increases

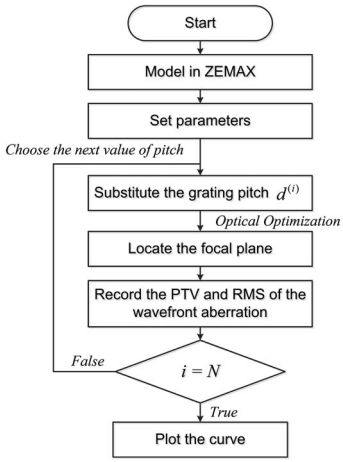

Fig. 6. Flowchart of the wavefront aberration analysis on the focal plane.

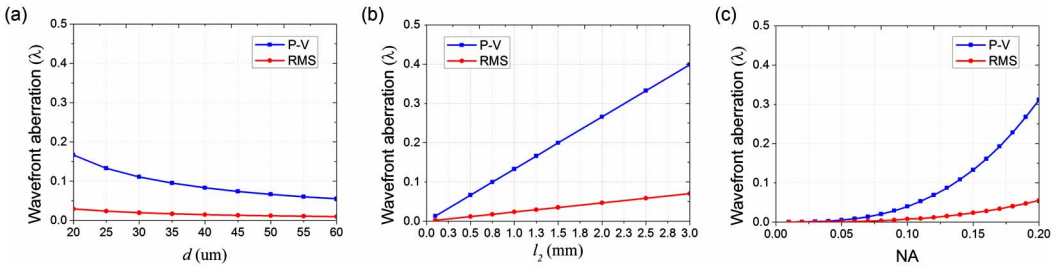

Fig. 7. Curves of wavefront aberration on the focal plane with the change of (a) the grating pitch, d, (b) the distance, l_2, from the cross grating to the order selection mask, and (c) the numerical aperture (NA) of the aplanatic lens.

linearly with the increase of the distance, l_2. In practice, this distance can hardly be less than 1 mm owing to the restriction of the adjustment mechanism. At the critical distance of 1 mm, the PTV and RMS of the wavefront aberration are, respectively, 0.1329λ and 0.0235λ with the grating pitch at 25 μm. When the grating pitch increases to 50 μm, the PTV and RMS of the focal plane aberration are 0.0664λ and 0.0117λ, respectively.

C. Influence of the Numerical Aperture of Aplanatic lens on the Focal Plane Aberration

In addition, the curve of the focal plane aberration with the change of numerical aperture is shown in Fig. 7(c). We can find that the wavefront aberration increase when the numerical aperture becomes larger, and the increasing rate is getting steeper and steeper. To control the system error of our wavefront diagnosis system, the numerical aperture of the aplanatic lens, NA, need to be less than 0.15.

D. Calibration of System Error

The advantage of using CGLSI for wavefront diagnosis is its common-path and self-reference features, which gives the test result high repeatability no matter how strong the environmental vibration is. However, the simulation above also shows that the cross grating will introduce an extra wavefront aberration into the test result. Moreover, as the position and tilt errors of components are inevitable in the alignment process, the system error may also result from the aberration and misalignment of the aplanatic lens, the tilt of the cross grating, and the tilt of the CCD imaging plane. For higher precision measurements, the system error should be eliminated as much as possible with the calibration method below.

For system error calibration, a collimator whose wavelength is 532 nm and the RMS of wavefront error better than $1/100\lambda$, is chosen to be tested by our CGLSI wavefront diagnosis system at first. Suppose that the system error is Δ. As the wavefront aberration of this collimator is very small, the test result of the collimator, W_c using our CGLSI wavefront diagnosis system can be described as

$$W_c = \Delta. \tag{17}$$

Assuming that the actual wavefront under test is W_{test}, and the test result, W, of our system measuring this wavefront can also be expressed as

$$W = W_{test} + \Delta. \tag{18}$$

Subtracting Eq. (18) from Eq. (17), we can obtain the wavefront distribution with system error calibration,

$$W_{test} = W - W_c, \tag{19}$$

where W_{test} is the final result of the wavefront under test, W is the test result of this wavefront using our system, and W_c is the test result of the collimator. As the environment vibration has little effect on our system error, the collimator need not be tested every time before our measurement. Actually, only when the testing environment is changed or any of the components is readjusted the collimator should be employed for error calibration, and then the wavefront data, W_c, can be stored in the computer for the following measurements.

5. Wavefront Retrieval of CGLSI Interferogram Using Differential Zernike Polynomials Fitting

After the interferogram is obtained by our CCD, the FFT and the differential Zernike polynomials fitting method can be employed for wavefront retrieval [27–29]. As is shown in Fig. 8, the interferogram is at first transformed into the Fourier spectrum by FFT. Then the $+1$ orders in the x and y directions are selected and transformed into the shearing wavefronts in the x and y directions by inverse fast Fourier transform (IFFT), respectively [30]. Last, the differential Zernike polynomials fitting method is employed to retrieve the actual wavefront distribution using these two orthogonal shearing wavefronts.

Supposing that the wavefront under test is $W(x,y)$, the two shearing wavefronts obtained by Fourier spectral filtering and IFFT can be expressed as

$$\begin{aligned}\Delta W_x(x,y) &= W\left(x-\frac{s}{2},y\right) - W\left(x+\frac{s}{2},y\right),\\ \Delta W_y(x,y) &= W\left(x,y-\frac{s}{2}\right) - W\left(x,y+\frac{s}{2}\right).\end{aligned} \tag{20}$$

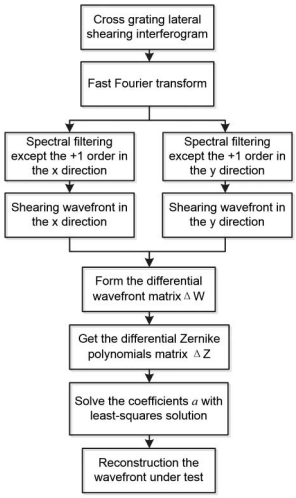

Fig. 8. Wavefront retrieval method using FFT and differential Zernike polynomials fitting.

In modal wavefront retrieval, the wavefront is decomposed into a set of basic functions, while Zernike polynomials are commonly used as the basic functions for this retrieval. The original wavefront $W(x,y)$ can be explained by N terms of Zernike polynomials in the following form,

$$W(x,y) = \sum_{j=1}^{N} a_j Z_j(x,y), \qquad j = 1,2,\ldots,N. \tag{21}$$

Substituting Eq. (21) into Eq. (20), the shearing wavefronts expressed in the form of Zernike polynomials can be obtained,

$$\Delta W_x(x,y) = \sum_{j=1}^{N} a_j \left[Z_j\left(x - \frac{s}{2}, y\right) - Z_j\left(x + \frac{s}{2}, y\right) \right],$$
$$\Delta W_y(x,y) = \sum_{j=1}^{N} a_j \left[Z_j\left(x, y - \frac{s}{2}\right) - Z_j\left(x, y + \frac{s}{2}\right) \right]. \tag{22}$$

If the differential Zernike polynomials are defined as

$$\Delta Z_x = Z_j\left(x - \frac{s}{2}, y\right) - Z_j\left(x + \frac{s}{2}, y\right),$$
$$\Delta Z_y = Z_j\left(x, y - \frac{s}{2}\right) - Z_j\left(x, y + \frac{s}{2}\right). \tag{23}$$

Then the shearing wavefronts $\Delta W_x(x,y)$ and $\Delta W_y(x,y)$ can be expressed as follows,

$$\Delta W_x(x,y) = \sum_{j=1}^{N} a_j \Delta Z_x,$$
$$\Delta W_y(x,y) = \sum_{j=1}^{N} a_j \Delta Z_y. \tag{24}$$

In matrix form, it can be written as

$$\Delta \mathbf{W} = \Delta \mathbf{Z} \mathbf{a}, \tag{25}$$

where

$$\Delta \mathbf{W} = \begin{pmatrix} \Delta \mathbf{W}_x \\ \Delta \mathbf{W}_y \end{pmatrix}, \qquad \Delta \mathbf{Z} = \begin{pmatrix} \Delta \mathbf{Z}_x \\ \Delta \mathbf{Z}_y \end{pmatrix}. \tag{26}$$

Now the coefficients of Zernike polynomials can be obtained with the least-squares solution of Eq. (25), that is,

$$\mathbf{a} = (\Delta \mathbf{Z}^T \Delta \mathbf{Z})^{-1} \Delta \mathbf{Z}^T \Delta \mathbf{W}. \tag{27}$$

Substituting the coefficients obtained from Eq. (27) into Eq. (21), we can finally retrieve the wavefront under test.

6. Simulation and Experiment Results

A. Simulation and Design of Grating and Order Selection Mask

The first step of building the wavefront diagnosis system based on CGLSI is the simulation and design of the cross grating and the order selection mask. To keep as much wavefront information as possible, the shear ratio needs to be limited to between 0.1 and 0.2. Once the shear ratio is chosen, the other parameters including the grating pitch and the position and the size of the order selection windows can then be determined. In our experiment, the wavelength of the testing beam is 532 nm, the aperture is 30 mm, and the height of the CCD imaging plane is 4.8 mm. In the tolerance of the adjustment mechanism, the distance between the cross grating and the order selection mask can be set at 1 mm, and the focal length of the aplanatic lens is 100 mm, due to the limitation of its numerical aperture being no larger than 0.15. Following the related derivation and analysis above, the parameters of cross grating and order selection mask we designed are shown in Table 1.

As the parameters of the cross grating and its corresponding order selection mask are all fixed once they have been fabricated, we should take multiple shear ratios into account in the simulation and designing process, which also offers us some different choices during the experiment. After these parameters are determined, the cross grating and the order selection mask can be fabricated out by the electron beam exposure method with high precision.

Table 1. Parameters of Grating and Order Selection Mask

Shear Ratio	Pitch d (μm)	d_{win} (μm)	D_{win} (μm)
0.1864	20	53.3	5.96
0.1494	25	42.7	5.70
0.0937	40	26.4	5.56
0.0751	50	21.6	5.32

B. Test Results of Wavefronts

A collimator whose wavelength is 532 nm and the RMS of wavefront error better than $1/100\lambda$ is employed in our experiment. The interferogram of this collimator, when the testing grating pitches are 25 and 50 μm, respectively, are shown in Figs. 9(a) and 9(b). We can find that the fringe spacing is larger when the grating pitch is at 50 μm, while the overlapped region of all the four diffraction beams, as is illustrated with the red dashed circle on the interferogram, is also larger at 50 μm, which shows that the shear ratio at 50 μm is relatively smaller than the shear ratio at 25 μm.

In order to facilitate the comparative experiment with the ZYGO interferometer, we place an optical

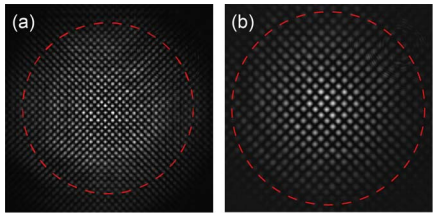

Fig. 9. Interferogram obtained by the CGLSI wavefront diagnosis system, (a) grating pitch at 25 μm and (b) grating pitch at 50 μm.

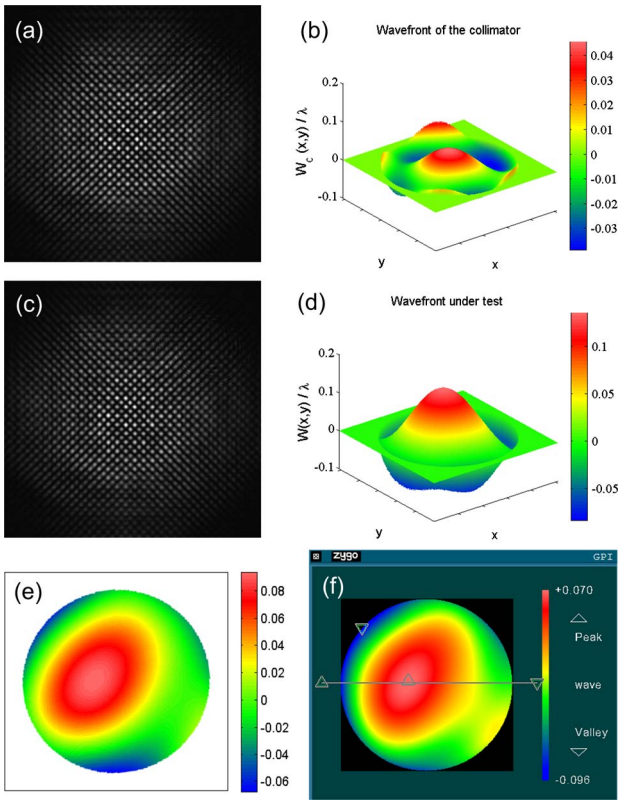

Fig. 10. Comparative experiment results with a ZYGO interferometer: (a) interferogram of the collimator, (b) wavefront of the collimator, (c) interferogram of the wavefront distortion caused by the optical flat, (d) wavefront distortion of the optical flat with no calibration, (e) calibrated wavefront distortion of the optical flat, and (f) test result of the same optical flat with a ZYGO GPI.

Table 2. Comparative Results between CGLSI and ZYGO GPI

	1	2	3	Average
CGLSI				
PTV (λ)	0.161	0.160	0.164	0.162
RMS (λ)	0.036	0.036	0.036	0.036
ZYGO GPI interferometer				
PTV (λ)	0.166	0.163	0.168	0.166
RMS (λ)	0.037	0.037	0.037	0.037

flat with certain surface error in front of the collimator so that the beam from the collimator is then distorted, which becomes our wavefront under test. The cross grating with 25 μm pitch and its corresponding order selection mask is employed to test the wavefront. For system error calibration, the collimator should be measured first. The interferogram of the collimator is shown in Fig. 10(a) and the wavefront, W_c, which indicates the system error, is retrieved using the differential Zernike polynomials fitting method in Fig. 10(b). The wavelengths, λ, of our results have all been converted to 632.8 nm for the comparison with the ZYGO GPI. Next, the interferogram of the beam distorted by the optical flat is shown in Fig. 10(c) and its test result, W, is in Fig. 10(d). Using the system error calibration method above, the final wavefront distortion measured, W_{test}, is shown in Fig. 10(e). Fig. 10(f) is the test result of the same optical flat using the ZYGO GPI interferometer, and with the multiple repeated experiments shown in Table 2, the CGLSI wavefront diagnosis system exhibits both high precision and repeatability. Note that the ZYGO GPI is placed on a vibration isolation platform while our CGLSI has no means of vibration isolation. This experiment shows that our wavefront diagnosis system based on CGLSI has the advantage of suppressing environmental vibration due to its common-path configuration.

7. Conclusion

A common-path cross-grating lateral shearing interferometer (CGLSI) able to measure both continuous and transient wavefronts is proposed in this paper. An aplanatic lens is employed to convert the wavefront under test into a convergent beam for CGLSI measurement. In the designing of our CGLSI wavefront diagnosis system, we have built a geometrical optics model for the determination of the grating pitch and a Fresnel diffraction model for the parameters of the order selection mask. The relationship between the shear ratio and the grating pitch has been obtained and the intensity on the order selection mask has been simulated out, which provide an important basis for the cross grating and order selection mask's design and fabrication. After the determination of all the parameters of components, we have made a detailed analysis of the influence of the grating pitch, the distance from the cross grating to the order selection mask, and the numerical aperture of the aplanatic lens on the system error. The smaller

the grating pitch, or the further the distance between the grating and the mask, or the larger the numerical aperture, will all result in a larger system error. To eliminate this error, a calibration method is introduced by employing a nearly ideal collimator whose RMS error is better than $1/100\lambda$. The test result of this collimator is obtained and then stored in the computer for calibration in the further measurement of other wavefronts. We have designed different grating pitches and their corresponding order selection masks before our experiment. The experimental results of an optical flat compared with a ZYGO interferometer shows that our wavefront diagnosis system is highly precise and has a nice repeatability.

Summarizing, the CGLSI wavefront diagnosis system is not only compact in mechanical structure but also exhibits the advantages of suppressing environmental vibration and ignoring the influence of the beam coherent length under testing. As a result, it can be applied to many different fields like precise fabrication of lithography lenses, high power lasers in the ICF system, and wavefront testing of hypersonic flow field.

This work was supported by the National Natural Science Foundation of China (11275172).

References

1. J. Primot, "Theoretical description of Shack–Hartmann wavefront sensor," Opt. Commun. **222**, 81–92 (2003).
2. J. Primot and N. Guérineau, "Extended Hartmann test based on the pseudoguiding property of a Hartmann mask completed by a phase chessboard," Appl. Opt. **39**, 5715–5720 (2000).
3. J. E. Millerd, N. J. Brock, J. B. Hayes, and J. C. Wyant, "Instantaneous phase-shift point-diffraction interferometer," Proc. SPIE **5531**, 264–272 (2004).
4. G. Rodriguez-Zurita, C. Meneses-Fabian, N. I. Toto-Arellano, J. F. Vazquez-Castillo, and C. Robledo-Sanchez, "One-shot phase-shifting phase-grating interferometry with modulation of polarization: case of four interferograms," Opt. Express **16**, 7806–7817 (2008).
5. D. I. Serrano-Garcia, N. I. Toto-Arellano, A. M. Garcia, J. A. R. Alvarez, A. Tellez-Quinones, and G. Rodriguez-Zurita, "Simultaneous phase-shifting cyclic interferometer for generation of lateral and radial shear," Rev. Mex. Fis. **57**, 255–258 (2011).
6. N. I. Toto-Arellano, G. Rodriguez-Zurita, C. Meneses-Fabian, and J. F. Vazquez-Castillo, "Phase shifts in the Fourier spectra of phase gratings and phase grids: an application for one-shot phase-shifting interferometry," Opt. Express **16**, 19330–19341 (2008).
7. J. C. Wyant, "Advances in interferometric metrology," Proc. SPIE **4927**, 154–162 (2002).
8. D. Malacara, *Optical Shop Testing*, 3rd ed. (Wiley, 2007), p. 165.
9. P. Hariharan and D. Sen, "Radial shearing interferometer," J. Sci. Instrum. **38**, 428 (1961).
10. T. Ling, D. Liu, Y. Yang, L. Sun, C. Tian, and Y. Shen, "Off-axis cyclic radial shearing interferometer for measurement of centrally blocked transient wavefront," Opt. Lett. **38**, 2493–2495 (2013).
11. D. Liu, Y. Yang, L. Wang, and Y. Zhuo, "Real time diagnosis of transient pulse laser with high repetition by radial shearing interferometer," Appl. Opt. **46**, 8305–8314 (2007).
12. K. A. Goldberg, P. Naulleau, S. Rekawa, P. Denham, J. A. Liddle, E. Anderson, K. Jackson, J. Bokor, and D. Attwood, "At-wavelength interferometry of high-NA diffraction-limited EUV optics," AIP Conf. Proc. **705**, 855–860 (2004).
13. M. Hasegawa, C. Ouchi, T. Hasegawa, S. Kato, A. Ohkubo, A. Suzuki, K. Sugisaki, M. Okada, K. Otaki, K. Murakami, J. Saito, M. Niibe, and M. Takeda, "Recent progress of EUV wavefront metrology in EUVA," Proc. SPIE **5533**, 27–36 (2004).
14. S. Kato, C. Ouchi, M. Hasegawa, A. Suzuki, T. Hasegawa, K. Sugisaki, M. Okada, Z. Yucong, K. Murakami, J. Saito, M. Niibe, and M. Takeda, "Comparison of EUV interferometry methods in EUVA project," Proc. SPIE **5751**, 110–117 (2005).
15. K. Murakami, J. Saito, K. Ota, H. Kondo, M. Ishii, J. Kawakami, T. Oshino, K. Sugisaki, Y. C. Zhu, M. Hasegawa, Y. Sekine, S. Takeuchi, C. Ouchi, O. Kakuchi, Y. Watanabe, T. Hasegawa, S. Hara, and A. Suzuki, "Development of an experimental EUV interferometer for benchmarking several EUV wavefront metrology schemes," Proc. SPIE **5037**, 257–264 (2003).
16. C. Ouchi, S. Kato, M. Hasegawa, T. Hasegawa, H. Yokota, K. Sugisaki, M. Okada, K. Murakami, J. Saito, M. Niibe, and M. Takeda, "EUV wavefront metrology at EUVA," Proc. SPIE **6152**, 61522O (2006).
17. Y. C. Zhu, K. Sugisaki, M. Okada, K. Otaki, Z. Q. Liu, M. Ishii, J. Kawakami, J. Saito, K. Murakami, C. Ouchi, M. Hasegawa, S. Kato, T. Hasegawa, A. Suzuki, and M. Niibe, "Experimental comparison of absolute PDI and lateral shearing interferometer," Proc. SPIE **5752**, 1192–1199 (2005).
18. J. Primot and L. Sogno, "Achromatic three-wave (or more) lateral shearing interferometer," J. Opt. Soc. Am. A **12**, 2679–2685 (1995).
19. S. Zhai, J. Ding, J. Chen, Y. Fan, and H. Wang, "Three-wave shearing interferometer based on spatial light modulator," Opt. Express **17**, 970–977 (2009).
20. P. Bon, G. Maucort, B. Wattellier, and S. Monneret, "Quadriwave lateral shearing interferometry for quantitative phase microscopy of living cells," Opt. Express **17**, 13080–13094 (2009).
21. S. Mousset, C. Rouyer, G. Marre, N. Blanchot, S. Montant, and B. Wattellier, "Piston measurement by quadriwave lateral shearing interferometry," Opt. Lett. **31**, 2634–2636 (2006).
22. S. Velghe, J. Primot, N. Guérineau, M. Cohen, and B. Wattellier, "Wave-front reconstruction from multidirectional phasederivatives generated by multilateral shearing interferometers," Opt. Lett. **30**, 245–247 (2005).
23. S. Velghe, J. Primot, N. Guérineau, R. Haidar, S. Demoustier, M. Cohen, and B. Wattellier, "Advanced wave-front sensing by quadri-wave lateral shearing interferometry," Proc. SPIE **6292**, 62920E (2006).
24. J.-C. F. Chanteloup and M. Cohen, "Compact, high resolution, four wave lateral shearing interferometer," Proc. SPIE **5252**, 282–292 (2004).
25. H. Wang, Y. Li, and K. Liu, "Approach to characterize manufacture tolerances of two-dimensional cross-phase grating," Opt. Eng. **52**, 104101 (2013).
26. L. Sun, D. Liu, T. Ling, and Y. Yang, "Mathematical modeling analysis on a small and compact two-dimensional CGLSI interference system," Proc. SPIE **8840**, 88400N (2013).
27. I. Agurok, "Method of 'truss' approximation in wave front testing," Proc. SPIE **3782**, 337–345 (1999).
28. F. Dai, F. Tang, X. Wang, O. Sasaki, and P. Feng, "Modal wavefront reconstruction based on Zernike polynomials for lateral shearing interferometry: comparisons of existing algorithms," Appl. Opt. **51**, 5028–5037 (2012).
29. T. Ling, D. Liu, L. Sun, Y. Yang, and Z. Cheng, "Wavefront retrieval for cross-grating lateral shearing interferometer based on differential Zernike polynomial fitting," Proc. SPIE **8838**, 88380J (2013).
30. M. Takeda, H. Ina, and S. Kobayashi, "Fourier-transform method of fringe-pattern analysis for computer-based topography and interferometry," J. Opt. Soc. Am. **72**, 156–160 (1982).